nuclear fusion

PAPER • OPEN ACCESS

Active tungsten expulsion in ELM-absent H-mode plasmas via on-demand ELM triggering with lithium granule injection

To cite this article: Z. Sun *et al* 2025 *Nucl. Fusion* **65** 106014

View the article online for updates and enhancements.

OPEN ACCESS
IOP Publishing | International Atomic Energy Agency
Nuclear Fusion
Nucl. Fusion **65** (2025) 106014 (18pp)
https://doi.org/10.1088/1741-4326/ae00dc

Active tungsten expulsion in ELM-absent H-mode plasmas via on-demand ELM triggering with lithium granule injection

Z. Sun[1], R. Maingi[1], Y.X. Cheng[2,*], Y.Z. Qian[3], W. Xu[3], Z. Wang[2], L. Zhang[2], A. Bortolon[1], Y.M. Duan[2], M. Huang[2], Y.F. Wang[2], J. Huang[2], T. Zhang[2], L. Chen[2], W. Wang[2], J.H. Yang[2], Y.Y. Li[4], D.G. Wu[2], K. Jia[2], H.L. Zhao[2], Q. Zhang[2], K. Tritz[5], H.Q. Wang[6], R. Lunsford[1], A. Nagy[1], A. Diallo[1], G.Z. Zuo[2,*], X.Z. Gong[2], J.S. Hu[2] and the EAST Team[2,a]

[1] Princeton Plasma Physics Laboratory, Princeton, NJ 08540, United States of America
[2] Chinese Academy of Sciences, Institute of Plasma Physics, Hefei 230031, China
[3] Hefei Comprehensive National Science Center, Institute of Energy, Hefei 230031, China
[4] Hebei Key Laboratory of Compact Fusion, Langfang 065001, China
[5] Johns Hopkins University, Baltimore, MD 21211, United States of America
[6] General Atomics, PO Box 85608, San Diego, CA 92186-5608, United States of America

E-mail: yunxing.cheng@ipp.ac.cn, zuoguizh@ipp.ac.cn and zsun@pppl.gov

Received 11 June 2025, revised 21 August 2025
Accepted for publication 29 August 2025
Published 11 September 2025

Abstract

Lithium granules gravitationally injected into the upper *X*-point region demonstrated on-demand edge-localized modes (ELM) triggering in otherwise ELM-suppressed H-mode plasmas on the Experimental Advanced Superconducting Tokamak. Sub-mm lithium granules dropped into enhanced D-alpha H-mode plasmas achieved a high triggering efficiency, while enabling ELM frequencies from several to hundreds of hertz. Core radiation from heavy impurities, dominated by W, was reduced by up to 60%, and the normalized energy confinement increased by up to 30%. At low injection frequencies, ELMs of substantially reduced size compared to spontaneous type-I ELMs were observed. At high injection frequencies, a transition to a mixed ELM phase occurred, characterized by intermittent larger ELMs and suppression of the quasi-coherent mode, achieving the most significant W reduction and energy confinement improvement. These results highlight a promising pathway for active W control via controlled, small ELMs in long-pulse, high-performance scenarios.

[a] See Gong *et al* 2024 (https://doi.org/10.1088/1741-4326/ad4270) for the EAST Team.
[*] Authors to whom any correspondence should be addressed.

Keywords: ELM, tungsten, lithium, pellet injection, EDA H-mode

(Some figures may appear in colour only in the online journal)

1. Introduction

The high-confinement mode (H-mode) is the standard operating scenario envisioned for future fusion reactors like ITER. It is characterized by the formation of a steep pressure gradient, or pedestal, at the plasma edge, leading to significantly enhanced energy confinement compared to the low-confinement mode (L-mode). However, the H-mode pedestal is often subject to periodic magnetohydrodynamic (MHD) instabilities known as edge-localized modes (ELMs) [1]. These ELMs manifest as transient bursts of energy and particles expelled from the plasma edge towards the plasma-facing components (PFCs). While ELMs can be beneficial for controlling plasma density and flushing impurities, particularly high-Z impurities, from the plasma edge and core [2–4], the large heat and particle fluxes associated with Type-I ELMs pose a significant challenge for the lifetime of PFCs in reactor-scale devices [5]. Consequently, substantial research efforts worldwide are dedicated to developing ELM control strategies, including ELM suppression or mitigation [6–9]. Several operational regimes have been discovered that exhibit intrinsically small or absent ELMs, such as the quasi-continuous exhaust (QCE) regime [10], the enhanced D_α (EDA) H-mode [11–15], I-mode [16], and QH-mode [17]. While these regimes alleviate the concerns associated with large ELM heat loads, the lack of periodic flushing mechanisms can potentially lead to the accumulation of impurities within the plasma core, especially high-Z materials originating from PFCs [18–20]. Indeed, impurity accumulation, particularly of high-Z elements, represents a significant potential limitation for achieving stationary high-performance plasmas in ELM-free or ELM-suppressed regimes. For instance, efforts to achieve high confinement via lithium wall conditioning on NSTX encountered challenges with impurity accumulation hindering steady-state operation [9, 21, 22]. Similarly, experiments exploring WPQH-mode with a tungsten divertor on DIII-D faced issues with tungsten penetration and accumulation, potentially limiting the compatibility of this regime with high-Z PFCs [23]. This underscores the critical need for effective impurity control strategies in advanced tokamak scenarios.

Tungsten (W) is a primary candidate material for PFCs, particularly in the divertor region of future fusion devices, owing to its high melting point, low sputtering yield, and low tritium retention [24]. However, W is a heavy element, and even trace amounts in the plasma core can lead to significant energy losses through line radiation, potentially degrading plasma performance and even causing radiative collapse [25]. In ELM-absent or type-I ELMy H-mode regimes, the neoclassical inward pinch often dominates W transport, leading to central accumulation, particularly when edge transport barriers are strong and core turbulence is weak [26]. Recent JET results show that an adequate ELM frequency is necessary to avoid W accumulation, which can further decrease ELM frequency and cause negative feedback on W expulsion [18]. While achieving favorable core temperature profiles (steep T_i gradient) can, in principle, lead to neoclassical temperature screening that counteracts the inward density pinch [27], reliance solely on screening may not be sufficient. Maintaining such profiles dynamically can be challenging, and source variations or transient events can still lead to unacceptable W levels. Therefore, active impurity expulsion mechanisms remain highly desirable, even in scenarios where temperature screening might be partially effective, to ensure robust W control during various plasma phases, including H-mode access and sustainment.

The controlled expulsion of impurities via small, frequent ELMs offers a potential solution. Such ELMs could provide the necessary impurity flushing to maintain high plasma purity, which is often correlated with accessing and sustaining high confinement levels without incurring the damaging heat loads of large Type-I ELMs. An alternative and potentially more flexible approach compared to passive regimes or RMP pacing is to actively trigger ELMs 'on-demand' when needed for impurity control. Pellet injection, typically used for fueling, has long been known to trigger ELMs [28]. Recent experiments have focused on using smaller pellets or granules specifically for ELM pacing or triggering [7, 29–34]. Injecting low-Z materials like lithium (Li) and boron (B) is particularly attractive due to their being solid at room temperature and their beneficial effects on wall conditioning [7]. Boron powder or granules injection is considered a real-time wall conditioning method for ITER [35, 36].

In this paper, we present experimental results from the Experimental Advanced Superconducting Tokamak (EAST) demonstrating a novel technique for active tungsten control in ELM-absent EDA H-mode plasmas. We utilized an impurity powder dropper (IPD) system to inject submillimeter-sized lithium granules near the upper *X*-point. This method successfully triggered controlled, typically small ELMs at frequencies determined by the injection frequencies. We show that this technique effectively reduces core tungsten concentration and associated radiative losses, leading to a significant improvement in energy confinement, without requiring large, potentially damaging ELMs. Section 2 describes the experimental setup, including the EAST device, key diagnostics, the IPD system, and the target plasma scenario. Section 3 presents the detailed experimental results, focusing on ELM triggering efficiency, the impact on W concentration and radiation, confinement enhancement, and the characteristics of the triggered ELMs. Section 4 discusses the potential mechanisms, compatibility with edge modes, and considers future prospects. Finally, section 5 provides a summary of the key findings.

2. Experiment setup

2.1. EAST description

The experiments were performed on EAST, which is a fully superconducting tokamak featuring a flexible poloidal field coil system enabling various plasma shapes, including upper-single null (USN), lower-single null (LSN), and double-null configurations. It is designed for long-pulse operation and high-performance H-mode studies relevant to ITER. EAST has a major radius $R \approx 1.85$ m and a minor radius $a \approx 0.45$ m. It can achieve a toroidal magnetic field (B_t) up to 3.5 T and a plasma current (I_p) up to 1 MA. The device is equipped with an ITER-like tungsten (W) divertor in the upper part and a graphite lower divertor (during the campaign reported here), allowing studies of plasma-material interactions with reactor-relevant materials. Heating and current drive systems include neutral beam injection (NBI, co- and counter-current capable), lower hybrid wave (LHW, at 2.45 GHz and 4.6 GHz), electron cyclotron heating (ECH, at 140 GHz), and ion cyclotron range of frequencies heating [37].

2.2. Diagnostics

A comprehensive suite of diagnostics was employed to monitor the plasma response to Li granule injection (figure 1). ELM activity was primarily monitored using fast magnetic pickup (Mirnov) coils distributed toroidally and poloidally to detect MHD precursors and crashes (dB/dt signals). Filter-scope arrays measuring D_α (656.3 nm) emission from the upper and lower divertor targets provided high time-resolution measurements of particle fluxes associated with ELMs. Langmuir probe arrays embedded in the upper and lower divertor targets measured the saturated ion current (J_{sat}), providing another indicator of particle expulsion during ELMs. The ELM size is often characterized by the peak amplitude of the D_α or J_{sat} spike during an ELM, relative to the baseline level between ELMs. The ablation of injected lithium granules was monitored using the same filter-scope system, specifically tracking Li-II emission at 548.5 nm, sharing the line-of-sight (LOS) with the D_α channels viewing the upper divertor region (e.g. U1, U13 in figure 1). Additionally, a fast visible-light camera provided qualitative images of the granule trajectory and ablation dynamics. Electron temperature (T_e) profiles were measured by a vertical Thomson scattering (TS) system. Due to calibration challenges during this campaign, density profiles (n_e) were obtained from a fast frequency-sweeping reflectometer covering the edge and core regions. Relative changes in T_e were also inferred from a multi-channel electron cyclotron emission (ECE) system, which is particularly useful for tracking fast temperature fluctuations during ELMs, though interpretation can be complex due to potential non-thermal electron populations generated by LHW heating. Ion temperature (T_i) and toroidal rotation profiles were measured using core charge exchange recombination spectroscopy (CXRS) based on intrinsic carbon impurity emission. Total radiated power (P_{rad}) and line-integrated radiation profiles were measured by a horizontal multi-LOS AXUV (Absolute eXtreme UltraViolet) bolometer system covering the entire poloidal cross-section (64 channels shown in figure 1, right). A vertical AXUV array was also available but had limited coverage. Tungsten behavior was investigated using an integrated suite comprising passive visible spectroscopy monitoring W-I emission (400.9 nm) from the upper W divertor outer target plate [38], two flat-field grazing incidence extreme ultraviolet (EUV) spectrometers (covering 1–13 nm and 2–50 nm) with fast- time response and 5 ms resolution [39], and a space-resolved EUV spectrometer (3–52 nm) measuring radial emission profiles of core W ions (e.g. W^{26+} to W^{45+}) over the range $Z = -23.4$ cm to $+23.8$ cm with ~200 ms resolution [40]. The volume-averaged tungsten concentration ($c_W = n_W/n_e$) presented in this paper was estimated using a robust method that relates the total radiated power from tungsten to the brightness of the unresolved transition array (W-UTA). This technique is preferred for tungsten analysis in EAST as it overcomes the significant limitations of the more traditional single-emission-line approach. The standard method, which relies on the intensity of a single, isolated line and its photon emissivity coefficient, is highly effective for impurities like molybdenum, which possess strong, well-isolated lines. However, for tungsten, the strong, isolated lines from high charge states (e.g. W XLIV, W XLVI) are only bright in high-temperature plasmas ($T_e > 2.0$–2.5 keV), while the lines from lower charge states are blended into the broad W-UTA feature, making them difficult to resolve accurately. Instead, our methodology leverages two key findings. First, during transient impurity events (e.g. Unidentified Flying Object-UFO), a strong and consistent empirical linear relationship is observed between the increase in total radiated power (ΔP_{rad}), measured by the bolometer, and the increase in the W-UTA intensity ($\Delta I_{W\text{-}UTA}$), measured by the EUV spectrometer ($P_W \approx 110 * I_{W-UTA}$). This relationship was calibrated across numerous EAST discharges with core temperatures ranging from 1 to over 4 keV, thereby inherently accounting for the temperature-dependent emissivity of the W-UTA. Second, this empirical result is equated with the theoretical definition of radiated power from the tungsten cooling rate, $L(T_e)$, where $P_W = \int c_W n_e^2 L(T_e)\,dV$. By equating the empirical measurement with the theoretical definition, a direct formula is derived to calculate the volume-averaged tungsten concentration: $c_W = 110 I_{W-UTA}/(\overline{n_e}^2 \int L(T_e)\,dV)$. While impurity transport coefficients (D and V) significantly alter the shape of the c_W profile, simulations confirm that their effect on the volume-averaged concentration is much weaker. This makes the method less sensitive to the unknown shot-to-shot transport details and ideal for fast, reliable, and quasi-real-time monitoring of the overall tungsten content. More information on this methodology is documented in the [41], and a similar technique is employed at ASDEX-Upgrade [42]. The W-UTA itself remains a prominent spectral feature even in

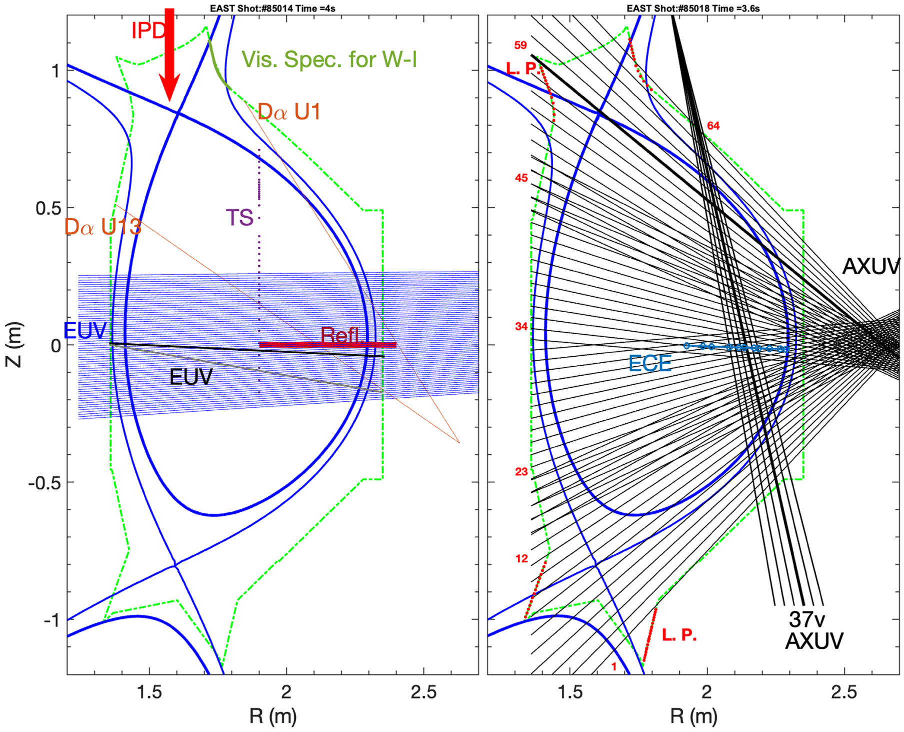

Figure 1. Schematic of the impurity powder dropper (IPD) and primary diagnostics employed in the experiments. The vertical red arrow highlights the path of falling Li granules from the IPD. The left side shows reconstructed equilibrium from discharge #85014@4 s, superimposed by monitor region from one visible W-I spectrometer, three flat-field EUV spectrometers, multiple Dα array labeled (e.g. U1, U13), Thomson scattering chords (TS), reflectometry (Refl.). The right side shows reconstructed equilibrium from discharge #85 018@3.6 s, overlaid by viewing lines of horizontal (labeled 64–1 from top to bottom) and vertical AXUV arrays.

high-temperature EAST plasmas, as shown in figure 3 of the [43].

2.3. Actuator setup: impurity powder dropper (IPD)

The key actuator for these experiments was the IPD [44] system installed on EAST. This system allows controlled delivery of various granular or powder materials into the plasma edge. For this study, Li granules with a nominal diameter of 0.7 ± 0.1 mm (corresponding to approximately 2.5×10^{19} electrons per granule if fully ionized) were used. The IPD was mounted on a top port (J-port) and utilized a vertical guiding tube (central location $R = 1.57$ m, diameter = 25 mm) to direct the granules towards the upper X-point region in the USN configuration employed. The granules fall primarily under gravity, reaching estimated velocities of $\sim$10 m s^{-1} near the plasma edge. The outflow rate is controlled by applying a voltage to piezoelectric elements that induce vibrations in the granule reservoir and trough. A modification involving a thin baffle welded onto the trough edge enabled operation in two distinct modes, depending on the driving voltage waveform applied to the piezoelectric actuators (figure 2).

In the discrete mode, achieved at lower or pulsed drive voltages, individual Li granules are dispensed sequentially, allowing for paced ELM triggering. Each granule enters the plasma, ablates, and produces a distinct, localized interaction. This is visualized as bright streaks in fast camera images (figure 2(*a*)) and corresponds to sharp, well-separated peaks in the Li-II emission signal measured by filter scopes viewing the ablation region (figure 2(*e*)). While the *average* injection frequency can be controlled, the release of individual granules in this mode is not strictly periodic due to the stochastic nature of granule flow at the baffle edge. In the continuous mode, achieved at higher sustained drive voltages, the granule flow rate increases significantly, resembling a powder flow and resulting in a more elevated, continuous Li-II signal (figure 2(*f*)). The visible camera shows a broader, more persistent ablation cloud (figures 2(*c*) and (*d*)). This flexibility allowed testing the plasma response to both isolated perturbations (discrete mode) and more sustained edge perturbations (continuous mode).

Previous work on EAST explored ELM triggering and mitigation with Li granules injected from the midplane locations [31–33, 45] and the X-point [7], providing valuable context for optimizing the injection location and granule size used here. Injecting near the X-point was chosen to maximize the perturbation effect from magnetic flux expansion in the pedestal foot/separatrix region while minimizing deep core penetration. We suppose the localized ablation cloud effectively creates a perturbation that is 'stretched' poloidally along the separatrix. This large-scale perturbation, situated directly at the plasma boundary, might be more effective at destabilizing ballooning modes compared to a more localized perturbation higher up on the pedestal shoulder introduced via midplane injection [34, 46].

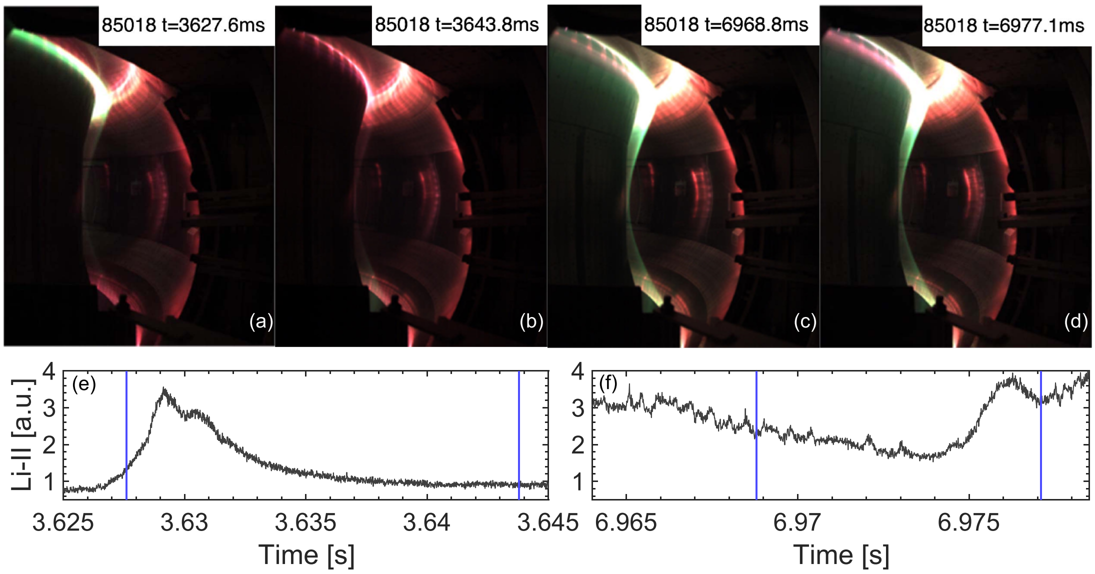

Figure 2. Visible true-color camera images of discrete (*a*), (*b*) and continuous (*c*), (*d*) Li granule injection from the upper divertor, together with the corresponding Li-II signals (*e*), (*f*). In discrete mode, each granule is clearly identifiable and produces distinct peaks in Li-II emission, whereas, in continuous mode, Li flows in a 'powder-like' manner, causing a continuous ablation profile and leveraged Li-II signal.

2.4. Plasma scenario

The experiments were conducted in USN H-mode discharges with the ion grad-B drift directed upwards, corresponding to the 'favorable' configuration for H-mode access with a lower L-H power threshold on EAST. The target regime was an EDA H-mode [11, 13], which is typically ELM-absent or exhibits only very small, high-frequency grassy ELMs [47]. EDA H-mode is characterized by relatively high edge density and the presence of a quasi-coherent mode (QCM) located in the pedestal region, which is believed to provide sufficient particle transport to prevent uncontrolled density rise [12, 48]. However, in EAST EDA H-modes with the W divertor [14], significant W accumulation is frequently observed in the absence of large ELMs and sufficient gas puff. The primary objective of these experiments was to utilize Li granule injection to systematically trigger ELMs in this otherwise ELM-absent EDA scenario to actively control and reduce W accumulation. Typical discharge parameters were: plasma current $I_p \approx 0.5$ MA, toroidal magnetic field $B_t \approx 2.4$ T on axis, safety factor at the 95% flux surface $q_{95} \approx 5.5$, plasma elongation $\kappa \approx 1.67$, and averaged triangularity $\delta \approx 0.41$. The total auxiliary heating power was maintained at approximately 5.2 MW, comprising 2.2 MW LHW @ 4.6 GHz, 0.8 MW LHW @ 2.45 GHz, 1.4 MW co-current NBI (beam NBI1L), and 0.8 MW ECH (140 GHz, centrally deposited). The line-averaged density, controlled via gas puff feedback, was typically around $n_{eL} \approx 4.0 \times 10^{19}$ m^{-3}.

3. Experimental results

This section details the experimental observations demonstrating the effectiveness of Li granule injection for triggering ELMs and controlling tungsten accumulation in EDA H-mode plasmas on EAST.

3.1. Induces ELMs, reduces radiation, and improves confinement in EDA H-mode

A clear demonstration of the technique's impact is provided by comparing a reference ELM-absent EDA H-mode discharge (#85014) with a discharge featuring Li granule injection (#85018), shown in figure 3. Both discharges maintained matched operational parameters like plasma current (I_p, panel a) and total auxiliary heating power (P_{total}, panel (*b*) with NBI from $t = 3$ s to 7 s. The reference discharge #85014 displays typical EDA characteristics for the period $t \approx 3$ s to approximately 6.5 s: stationary line-averaged density (n_{eL}, panel (*d*), stored energy (W_{MHD}, panel (*e*), and bulk radiation ($P_{rad\text{-}bulk}$, panel (*c*). However, during this ELM-absent phase, the tungsten concentration (c_W, panel (*g*), estimated from EUV spectroscopy, shows a gradual increase, signaling detrimental impurity accumulation. The radiation power from bulk plasma takes over ~50%–60% of the absorbed heating power. The D_α emission signal (panel (*h*), blue) is elevated after the L-H transition at $t \approx 2.15$ s and relatively quiescent, lacking the large spikes characteristic of Type-I ELMs. Cross-spectrogram analysis of density and temperature fluctuations (panel l) confirms the presence of the signature EDA QCM during this period. Later in the discharge ($t > 6.5$ s), spontaneous mixed ELMs appear in #85014, correlating with a reduction in W concentration and an obvious improvement in confinement (panel f). The QCM amplitude was reduced just before the mixed ELM phase, which was accompanied by the appearance of small ELMs.

In sharp contrast, Li granule injection was initiated in discharge #85018 at $t \approx 3.6$ s. The plasma response evolved

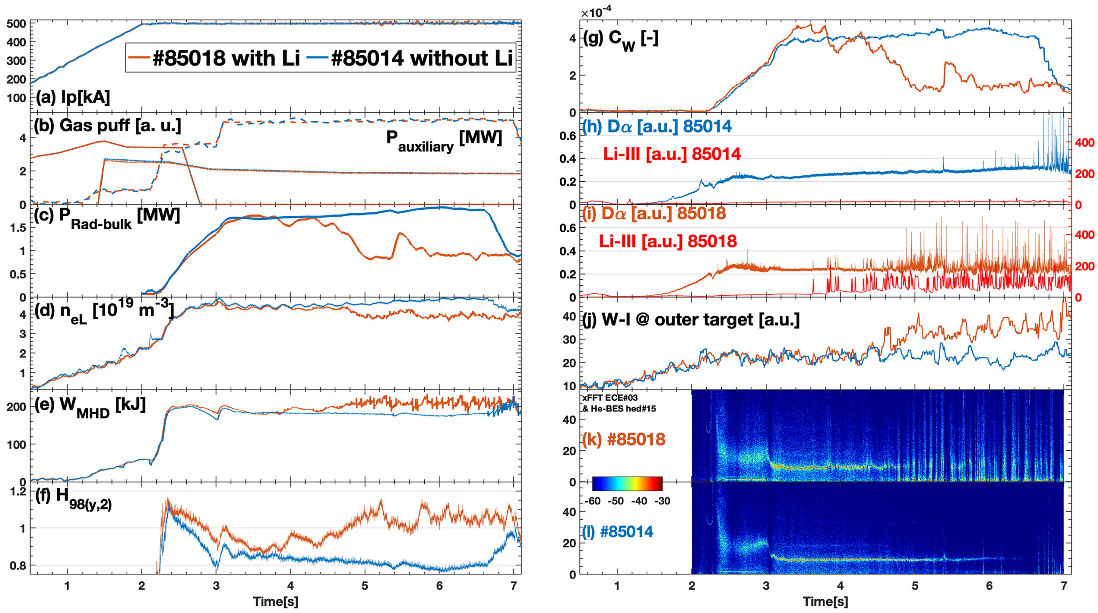

Figure 3. Time traces comparing the no-Li reference (#85014 blue) EDA H-mode to a discharge with Li granule injection (#85018 orange): (*a*) plasma current, (*b*) total auxiliary power (dashed line) and control voltage of gas fueling, (*c*) radiation power from the bulk plasma, (*d*) line-averaged density, (*e*) stored energy from EFIT, (f) H98(y,2) factor, (*g*) estimated core W concentration (from EUV UTA), (*h*) Dα emission (upper divertor) and Li-III by EUV for #85014, (*i*) Dα emission (upper divertor) and Li-III for #85018, (*j*) W-I emission from the upper outer target, and cross-power spectrograms between ECE channel#03 and He-BES channel Hed#15 for these discharges without (*l*) and with (*k*) Li injection, showing the QCM.

through distinct phases determined by the injection mode. The pre-injection **Phase I ($t < 3.6$ s)** mirrored the reference discharge, exhibiting W accumulation (panel g) and a baseline confinement factor H98(y,2) $\approx$ 0.87 (panel f). Upon initiation of **Phase II ($t \approx 3.6$ s–4.7 s)**, characterized by discrete granule injection (distinct Li-III spikes in panel i, red), small ELMs were reliably triggered with nearly 100% efficiency, as evidenced by the tightly correlated D_α spikes (panel i, orange). Notably, during this phase, the triggered small ELMs appeared to coexist with the QCM. The rate of W accumulation ceased, and C_W began to decline moderately (panel g). Correspondingly, core radiation decreased (panel c), and both stored energy and the H98 factor started to increase (panels e, f). The average ELM frequency, dictated by the injection rate, was approximately 50 Hz. A transition occurred around $t \approx 4.7$ s to **Phase III ($t \approx 4.7$ s–7.0 s)**, where the injection mode was switched to continuous delivery. This resulted in a significant increase in ELM frequency and a shift to a 'mixed ELM' regime, comprising a background of small ELMs interspersed with larger, irregular ELM events (panel i). A striking change during this phase was the strong mitigation or complete disappearance of the QCM (panel (*k*). Concurrently, the W concentration experienced a dramatic reduction, dropping by up to 60% from its peak value (panel (*g*), accompanied by a substantial decrease in core radiated power (panel (*c*). This reduction in radiative losses fueled a significant rise in stored energy (panel e) and a remarkable enhancement in energy confinement, with H98(y,2) reaching a sustained level of approximately 1.12 (panel (*f*). The substantial improvement in H98 strongly correlates with the decrease in P_{rad}, suggesting that mitigating core radiation is the dominant factor behind the confinement enhancement. Throughout Phases II and III, the line-averaged plasma density shows a slight decrease of about 7% compared to the pre-injection level (panel (*d*), remaining stable. This lack of density increase suggests that the particle source from the ablating granules is effectively balanced or exceeded by the particle expulsion from the triggered ELMs, indicating minimal net fueling from the injection, a point further discussed later. Interestingly, the averaged W-I emission monitoring the outer divertor source (panel (*j*) showed an increase during Phase III, implying that the more intense ELM activity might enhance gross W sputtering at the attached target with the peak electron temperature ~40–45 eV. Though Li ions can follow the magnetic field lines and deposit on the target to shield it from sputtering caused by incoming ions.

3.2. Reproducible ELM triggering and tungsten control

The effectiveness and reproducibility of the Li granule injection technique were confirmed across multiple discharges, as shown in figure 4. Discharge #85013 (panels (*a1*)–(*a2*)) and its repeat #85022 (panels (*f1*)–(*f2*)) without Li injection consistently showed initial W accumulation followed by large spontaneous ELMs or mixed ELMs. Another reference discharge, #85021 (panels (*e1*)–(*e2*)), reproduced the ELM-absent EDA behavior seen in #85014 (omitted in figure 4). These baseline discharges confirm the underlying plasma behavior and establish that the ELM triggering and subsequent W control observed in other discharges are direct consequences of the Li granule injection. Discharges employing discrete Li injection throughout the analyzed period, like #85017 (panels (*b1*)–(*b2*)) and #85016 (shown later in figure 9), demonstrated

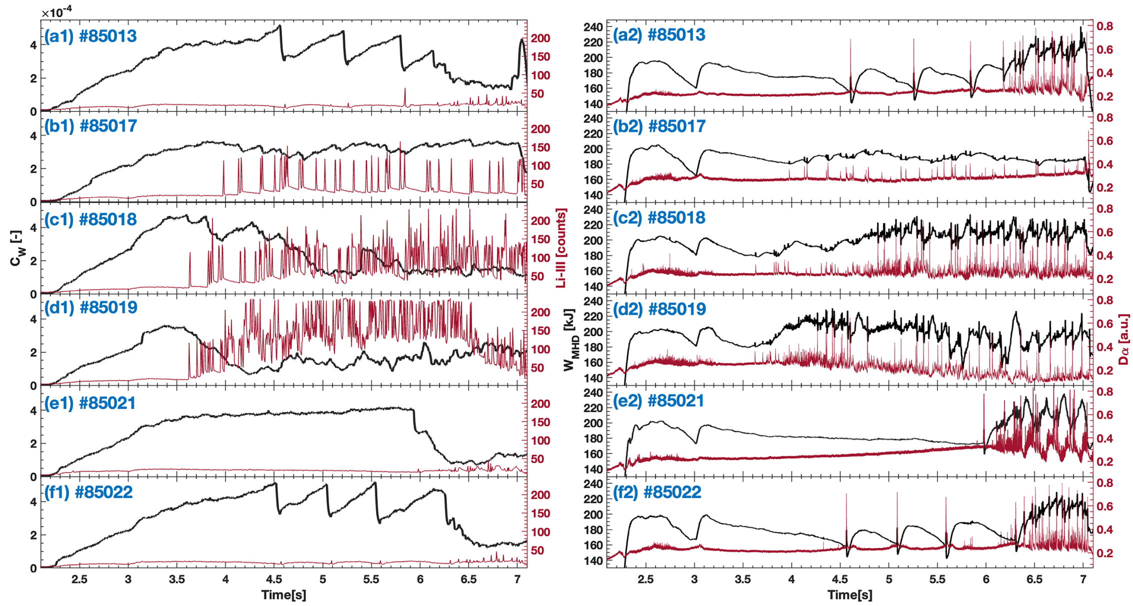

Figure 4. Discharge-to-discharge reproducibility of Li granule injection for ELM triggering. The left panels (1) display the evolutions of estimated W concentration (black) and Li-III emission (red, arbitrary units). The right panels (2) show D_α signals from the upper divertor (red), revealing ELM occurrence, and the plasma stored energy (black). Each row tracks a different discharge. (*a*) #85013: No Li injection, W build-up, then spontaneous large ELMs. (*b*) #85017: Discrete Li injection, pacing small ELMs. (*c*) #85018: Discrete then continuous Li injection (∼4.7 s transition). (*d*) #85019: Discrete then earlier continuous Li injection (∼4.2 s transition), causing earlier mixed ELM phase onset. (*e*) #85021: No Li injection, ELM-absent EDA (similar to #85014). (*f*) #85022: Repeat of #85013 without Li injection, showing similar behavior. Note: #85016 (discrete injection) is shown in figure 9.

the successful pacing of small ELMs. In these cases, regular D_α spikes (e.g. panel (*b2*), black) are clearly synchronized with the Li-II ablation signals (panel (*b1*), red), resulting in sustained operation with moderately low W concentration (panel (*b1*), blue) and good stored energy (panel b2, orange), crucially avoiding the large ELM excursions seen in the baseline discharges. The causality between the injection parameters and plasma response is further highlighted by comparing #85018 (panels (*c1*)–(*c2*)) and #85019 (panels (*d1*)–(*d2*)). Both discharges transitioned from discrete to continuous Li injection, but this transition was initiated earlier in #85019 (∼4.2 s) compared to #85018 (∼4.7 s). As a direct result, the onset of the mixed ELM phase (panel (*d2*) vs (*c2*)) and the associated rapid decrease in W concentration (panel (*d1*) vs (*c1*)) occurred correspondingly earlier in #85019. This demonstrates a clear control linkage: adjusting the Li injection mode and timing directly determines the evolution of the ELM regime and the effectiveness of W expulsion. Collectively, these comparisons across multiple discharges underscore that Li granule injection near the *X*-point provides a robust and reproducible means to trigger ELMs, where the frequency, size, and resulting impurity control level can be actively manipulated by tailoring the injection rate and mode.

3.3. Comparison of tungsten concentration between ELM-absent and induced ELM phases

The reduction in tungsten concentration was confirmed by space-resolved EUV diagnostics. Figure 5 compares radial profiles of line-integrated radiation (from horizontal AXUV) and emission brightness of specific W ions (from EUV spectrometer) between the ELM-absent phase (#85018, t = 3.6–3.75 s, red) and the Li-triggered mixed ELM phase (#85018, t = 5.0–5.15 s, blue). The AXUV radiation profiles (figure 5(*a*)) clearly show reduced emission across the cross-section except for chords viewing through the upper *X*-point, consistent with impurity removal from the main plasma and Li injection from the *X*-point. The space-resolved EUV spectrometer data provide more direct evidence by tracking individual W charge states. The radial locations of these charge states are primarily determined by the local electron temperature, a relationship illustrated by the fractional abundance calculation shown in figure 5(*e*). This distribution was calculated assuming coronal equilibrium using ionization and recombination rate coefficients from the ADAS database [49]. Specifically, the calculation utilizes the ionization coefficients from Loch *et al*. [50] (ADAS data type 'ADF11', file 'scd50_w.dat') and recombination coefficients from Pütterich *et al* [51] (ADAS data type 'ADF11', file 'acd50_w.dat'). The resulting fractional abundances align well with previous benchmark studies by Fujii *et al* [52] and Oishi *et al* [53], providing confidence in this theoretical mapping of ion locations. It is worth noting that while this calculation shows a somewhat broader radial distribution for the lower charge states (e.g. W^{26+}, W^{27+}), the fundamental spatial grouping of ions remains robust and is supported by direct experimental measurements of W ion distributions under similar plasma conditions [43]. Note that the distribution serves as a rough indicator since the calculation excludes effects such as transport, rotation, and other factors.

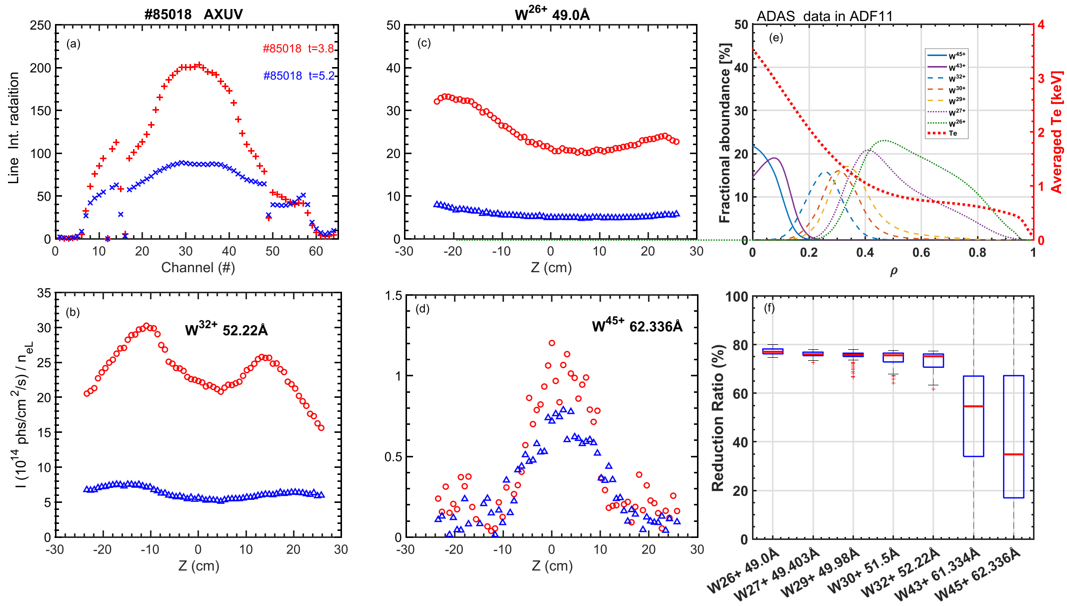

Figure 5. (*a*) Line-integrated radiation profiles from horizontal AXUV bolometry during the ELM-absent phase (#85018, t = 3.6–3.75 s, blue) and the induced mixed ELM phase (#85018, t = 5.0–5.15 s, red). (*b*)–(*d*) Radial profiles of emission intensity for representative ionized tungsten charge states (e.g. grouped by core W^{43+}–W^{45+}, mid-radius W^{29+}–W^{42+}, outer-region W^{26+}–W^{27+}) measured by the EUV spectrometer during the same time windows. (*e*) Example calculation of W ion fractional abundance distribution based on the measured T_e profile (from figure 6) using ADAS (assuming coronal equilibrium, no transport). (*f*) Reduction percentage of density-normalized W emission intensity for various charge states from the ELM-absent phase to the mixed ELM phase, highlighting significant W expulsion across multiple radial locations. The figure is a standard box plot where the central red line indicates the median, the blue box represents the interquartile range (25th to 75th percentiles), and the black dashed error bars (whiskers) show the extent of the non-outlier data.

Significant reductions in emission brightness (normalized with the line averaged density) during the mixed ELM phase (blue traces) compared to the ELM-absent phase (red traces) are observed for representative W ions residing in the core (W^{43+}–W^{45+}, panel d), mid-radius (W^{29+}–W^{42+}, panel b), and outer regions (W^{26+}–W^{27+}, panel c). To quantify this, figure 5(*f*) shows the reduction percentage of the density-normalized W emission intensity for various charge states. The box plots take data from all chords of the space-resolved EUV spectrometer (figure 1(*a*)). Substantial reductions, ranging from approximately 35% to 75%, are seen across the measured spectrum. This confirms that the ELM activity induced by Li granule injection effectively flushes tungsten not only from the edge but also from the pedestal and deep core regions where it poses the greatest threat through radiative losses.

3.4. Plasma profile changes associated with tungsten reduction

The expulsion of tungsten and the associated decrease in radiative power loss led to notable modifications in the plasma kinetic profiles, as shown in figure 6. This figure compares profiles from the ELM-absent phase (phase I) with those from the Li-triggered mixed ELM phase (phase III). Note that the induced mixed ELM phase shares similarities with the spontaneous mixed ELM phase. Panel (a) displays the electron density profiles measured by reflectometry. During the mixed ELM phase (red), the pedestal density ($\rho > \sim 0.8$) is notably lower ($\sim$8%–10%) compared to the ELM-absent phase (blue). The reflectometer measurement for the red profile did not fully penetrate to the deep core ($\rho < \sim 0.3$) in this specific time slice. Panel (b) depicts the T_e profile. Core T_e data is from TS, and checked against ECE. Due to an optical issue, edge TS channels were unavailable; the edge/pedestal T_e profile is reconstructed using an assumed value near the last closed flux surface (T_e@LCFS $\approx$ 90 eV) and the measured pedestal top temperature from reliable TS/ECE channels. The profile shows a substantial increase in core T_e (by $\sim$50% centrally) during the mixed ELM phase (blue). Panel (c) shows the ion temperature (T_i) profile measured by core CXRS. Only core data ($\rho < \sim 0.4$) is available. The edge T_i (dashed line) is assumed to be similar to the reconstructed T_e profile. A significant increase in core T_i (by 20–40%) is observed during the mixed ELM phase (blue). These profile changes—higher core T_e and T_i, and lower pedestal n_e—are consistent with reduced radiative cooling due to W expulsion, allowing auxiliary heating power to more effectively heat the plasma rather than being radiated away.

Furthermore, the observed pedestal profile changes—specifically the combination of steeper pedestal temperature gradients and reduced pedestal density—are theoretically favorable for mitigating high-Z impurity from SOL or divertor to the pedestal region via neoclassical transport effects,

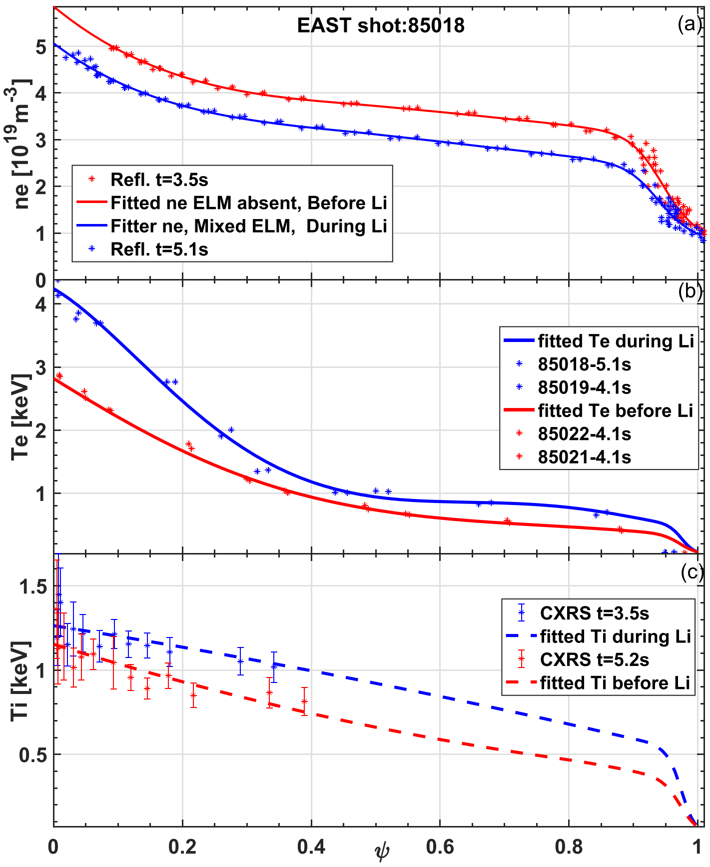

Figure 6. Electron temperature and density profiles from reference and Li granule injection discharges; blue and red colors represent ELM-absent and mixed ELM phases, respectively. The solid or dashed lines are fitted from scattered data or are assumed. Plasma profiles comparing the ELM-absent phase (blue, #85014@4 s) and the Li-triggered mixed ELM phase (red, #85018@5 s). (*a*) Electron density (n_e) from reflectometry (note limited core penetration for red profile). (*b*) Electron temperature (T_e) from TS (core) and ECE check; edge TS data omitted, pedestal fitted using LCFS value and measured top (dashed lines). (*c*) Ion temperature (T_i) from core CXRS; edge assumed same as T_e (dashed lines). Profiles show increased core T_e & T_i and reduced pedestal n_e during the mixed ELM phase. Solid/dashed lines are fits/interpolations/assumptions based on available data points (markers).

$V_{NC} \propto Zq^2\ (R/2L_{Ti} - R/L_{ne})$ [54]. Neoclassical transport theory predicts an inward pinch velocity for heavy impurities that is driven by the main ion density gradient and counteracted by the temperature gradient (via the thermal screening effect). The profile changes potentially create a positive feedback loop that complements the direct ELM flushing.

The observed mitigation of the QCM during the mixed ELM phase (figure 3(*k*)) also suggests a change in the underlying transport dynamics. QCMs are typically associated with particle transport and can be sensitive to changes in the edge density and temperature profiles [14]. Replacing this continuous transport channel with the intermittent transport bursts from ELMs leads to the observed lower pedestal density. However, the evolution of pedestal density and temperature profiles can induce ELM appearance.

3.5. Characteristics of triggered ELMs: size, frequency, and dynamics

A crucial aspect of this technique is the ability to generate ELMs with characteristics distinct from spontaneous Type-I ELMs. Figure 7 displays the ELM size, represented by the peak D_α amplitude increase, versus the instantaneous ELM frequency (inverse time between ELMs). ELMs triggered during the discrete injection phases (#85016, #85017, #85018 Phase II, orange symbols) are distributed at a wide range of frequencies up to transient bursts near 250 Hz and possess significantly smaller amplitudes compared to typical spontaneous Type-I ELMs. In contrast, the larger ELMs observed during the induced mixed ELM phase (#85018 Phase III, green stars) exhibit amplitudes closer to spontaneous ELMs but are interspersed within the high-frequency background of smaller events. This clearly demonstrates that the Li granule injection rate provides direct, external control over the ELM frequency, enabling operation in a regime of frequent, small ELMs. Notably, the triggered ELM amplitude in the pacing regime remains small, offering a potentially benign mechanism for impurity control. The paced small ELM combined with QCM allows the decoupling of the ELM frequency from the size, moving away from the typical scaling observed for spontaneous ELMs. This external control is a key advantage of the technique. Note that the ELM sizes calculated from the D_α peak and baseline are consistent with the ion saturated current, the drop percentage of pedestal ECE, and the total

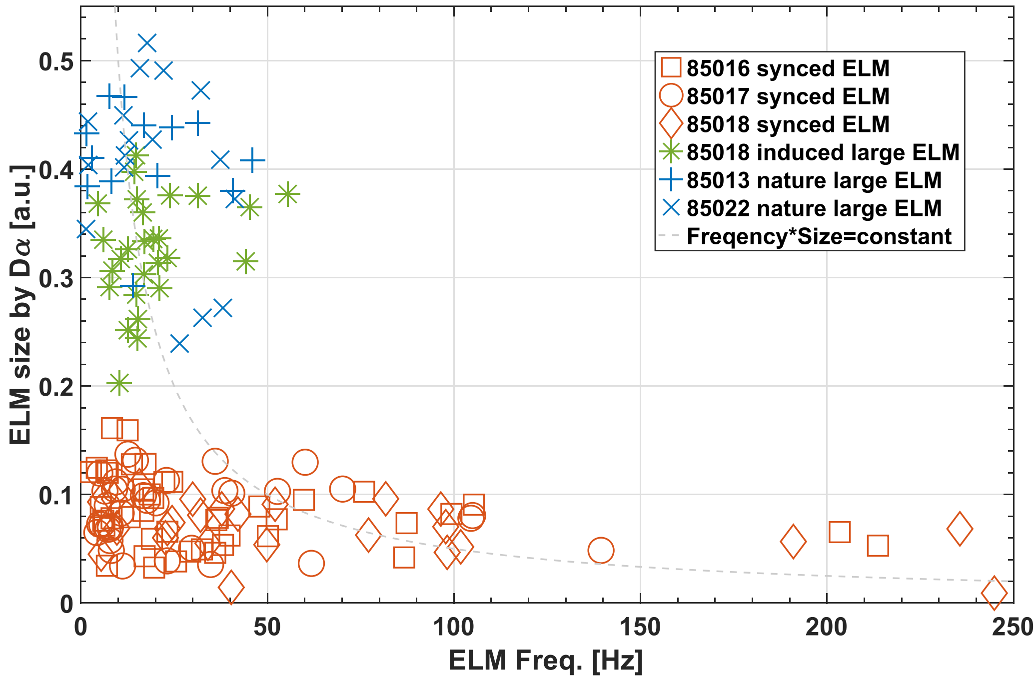

Figure 7. ELM size (relative D-alpha amplitude) versus instantaneous ELM frequency for different experimental discharges and phases. Orange symbols represent synced small ELMs triggered by discrete Li injection (from #85016, #85017, #85018 Phase II). Green stars represent the larger ELMs observed during the induced mixed ELM phase (from #85018 Phase III). High frequencies (>50 Hz) are achieved with small triggered ELMs.

stored energy. For the larger ELM, the stored energy drops 6%–10%, with a small ELM drop of less than 2%. In this context, 'synced' ELMs refer to events during the discrete injection phase where a clear one-to-one causal link exists between a single granule and a triggered ELM. 'Induced' ELMs, in contrast, refer to the ELMs observed during the continuous injection phase. Here, the plasma edge is modified by the constant stream of granules, which induces a state of frequent ELMing, but individual ELMs cannot be correlated with individual granules.

The dynamics of the triggering process are revealed in the zoomed-in time traces of figure 8. A successfully triggered small ELM (#85016@5.903s, orange lines in left panels) shows a rapid sequence: line-integrated radiation viewing through the *X*-point (#57) rises as the granule is ionized (panel a1), followed within approximately 4 ms by a distinct spike in the magnetic perturbation (panel (*b1*)), simultaneous increases in divertor D-alpha (panel (*d1*)) and Langmuir probe J_{sat} (panel (*e1*)), and measurable drops in stored energy (panel (*c1*)) and edge/core electron temperature (panel (*f1*), ECE). Critically, this ELM event correlates with a small but noticeable drop in the W concentration (g). Conversely, an instance where a granule injection failed to trigger an ELM (#85016@5.789s, left panels) shows the Li-II ablation signal but lacks the subsequent MHD activity and W expulsion. Such failed triggers were rare (<5%) and associated with smaller Li emissions (figure 9(*a*)). A reasonable explanation is that the granule size was not perfectly screened. In this case, despite the Li ablation, there are no corresponding spikes in d*B*/d*t*, D-alpha, or J_{sat} and no drops in W_{MHD}, ECE, or W concentration. The second rapid rise in D-alpha at $t \approx 1$ ms and the AXUV at $t \approx -0.5$ ms is commonly seen in the triggered ELM, identifying it as the start time of the ELM crash. The AXUV channel (#57) shows the fastest response to the granule ablation, even a few microseconds earlier than Li-II emission pointing to the upper divertor, possibly due to the toroidal locations of IPD, Filterscope, and bolometer. Before the nonlinear crash, the observed rise in AXUV, D_α, and J_{sat} can result from granule ablation. Assuming a granule velocity of $\sim$10 m s^{-1} in the path, an approximate 4-ms interaction time suggests the granule penetrates $\sim$4 cm into the plasma scrape-off layer or edge pedestal before triggering the ELM. The triggering suggests rapid destabilization near the edge. For comparison, a spontaneous small ELM with $\sim$20% smaller size from the reference discharge (#85014@6.156s, right panels) exhibits similar plasma parameter excursions (dB/dt, W_{MHD}, ECE, D_α, J_{sat}), but no significant AXUV and Li-II emission spikes. It also produces an obvious single-event drop in W concentration.

3.6. *Impact of ELM frequency and size on tungsten expulsion*

The effectiveness of ELMs in controlling tungsten accumulation depends on both their size (how much W is expelled per ELM) and their frequency (how often expulsion occurs). Figure 9 focuses on discharge #85016, which operated in the small-ELM pacing regime. Panel (*a*) shows the Li-II signal (black), indicating discrete granule injections, and the

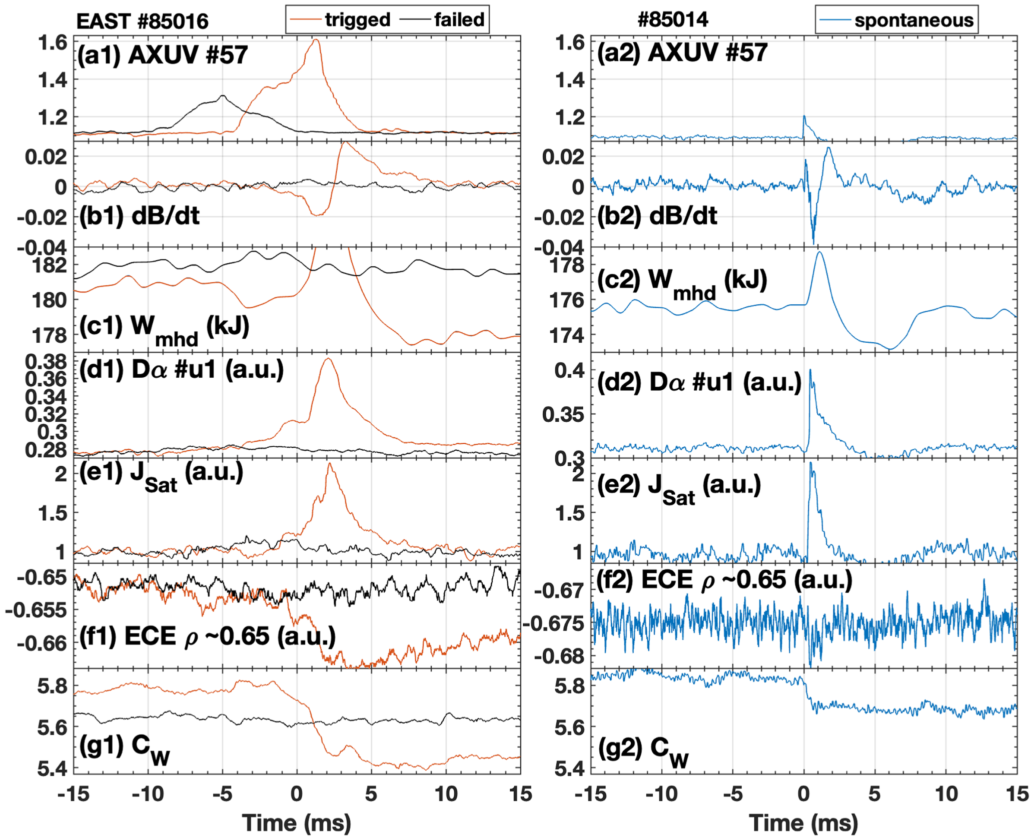

Figure 8. Zoomed-in time traces around single Li granule injection events. Left orange: Successful triggering of a small ELM in #85016 (t ≈ 5.903 s). Left black: A granule injection event in #85016 (t ≈ 5.789 s) that failed to trigger an ELM. Right: A spontaneous large ELM in the reference discharge #85014 (t ≈ 6.156 s) for comparison. Panels show: (*a*) AXUV signal viewing ablation region (channel #57 from figure 1); (*b*) Mirnov probe signal (dB/dt); (*c*) Plasma stored energy (W_{MHD}); (*d*) Divertor D-alpha emission; (*e*) Divertor Langmuir probe ion saturation current (J_{sat}); (*f*) ECE signal indicating T_e near ρ ≈ 0.65; (*g*) Estimated W concentration. Note the prompt ELM crash (∼4 ms after AXUV rise) and W drop in the successfully triggered case (left). The *Y*-axis scales are consistent across the left and right panels for each row.

plasma stored energy (orange). Panel (*b*) shows an AXUV signal viewing the low-field side plasma (black), the estimated W concentration (orange), and also Molybdenum (Mo) concentration (yellow, another intrinsic impurity). Nearly every significant Li-II spike is followed by a small drop in stored energy (a) and a clear dip in the W concentration (b, orange). This demonstrates the direct correlation: each triggered small ELM expels a measurable amount of tungsten. The two instances where small Li-II spikes did *not* trigger an ELM ($t \approx 5.19$ s and 5.78 s, corresponding to the failed trigger event in figure 8, black lines) show no corresponding dip in W concentration, reinforcing that the ELM itself is necessary for the expulsion. While each small ELM only removes a small amount of W, its high frequency prevents the accumulation seen in ELM-absent phases. For comparison, three naturally occurring large ELMs that occur spontaneously at $t \approx 6.88$ s, $t \approx 6.91$ s, and $t \approx 6.98$ s expel more W per event but disrupt the plasma more significantly (larger W_{MHD} drop, ∼7% versus <2%) and occur less frequently. The Mo concentration (intrinsic from other PFCs) also shows a similar expulsion behavior to that correlated with ELMs.

Figure 10 further explores the relationship between ELM characteristics, W control, and confinement across multiple discharges and conditions. Panel (a) plots the fractional W reduction per ELM versus ELM size (D-alpha amplitude). While there is significant scatter, a general trend emerges: larger ELMs (blue markers: natural; green markers: induced large) tend to expel a larger fraction of W per event compared to the triggered small ELMs (orange markers). However, the more critical factor for overall impurity control appears to be frequency. Panel (*b*) plots the estimated W concentration achieved against the average ELM frequency. A clear inverse relationship is observed—higher ELM frequencies consistently lead to lower W levels. This strongly indicates that maintaining a sufficiently high ELM frequency (above ≈ 50–100 Hz in these experiments) is essential for effective W management. The W influx (or recovery) between two triggered ELMs is observed in figure 9. Although the time-averaged W influx between ELMs increases with ELM frequency, it is saturated around 40 Hz from discharge #85016, #85017, and #85018. The triggered small ELMs (orange), despite their lower per-event efficiency (panel a), achieve excellent W

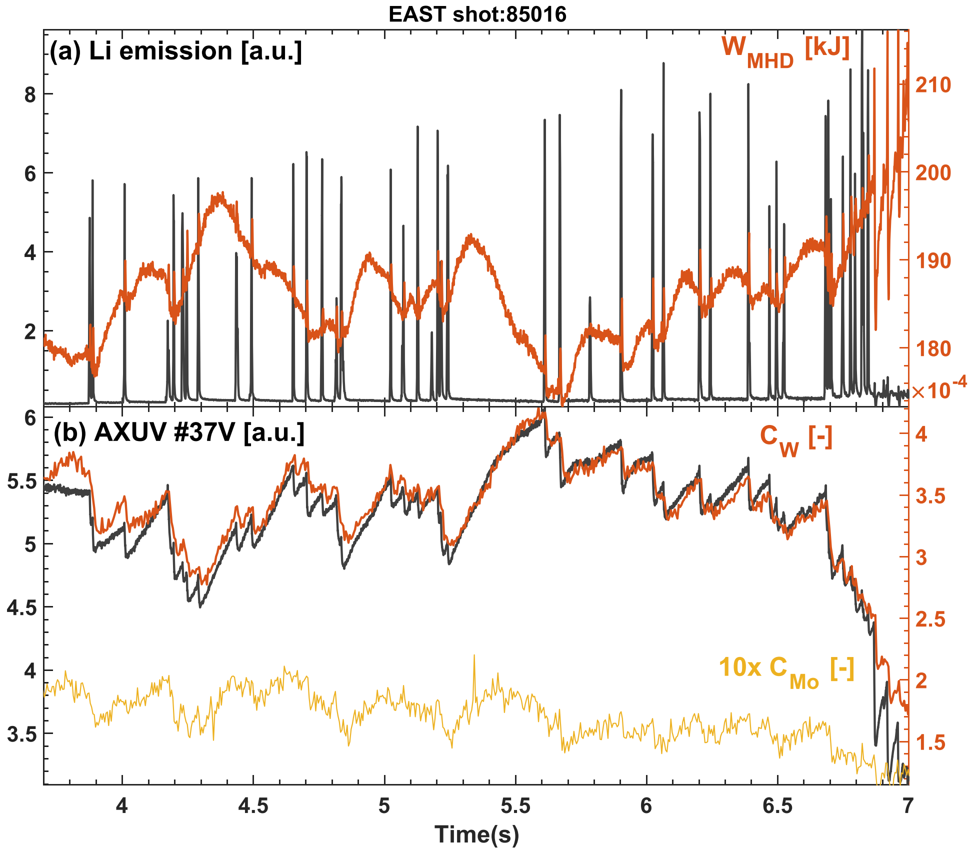

Figure 9. Time traces of (*a*) Li-II ablation emission (black) and plasma stored energy (orange), (*b*) AXUV pointing to low field side plasma (black), tungsten concentration (orange), and Mo concentration (yellow). Each Li granule injection triggers a small ELM, except for two small Li-II spikes at times ≈ 5.19 s and ≈ 5.78 s. Each ELM correlates with a dip in tungsten concentration. Natural large ELMs occur from time ≈ 6.88 s without substantial Li-II emission.

control due to their high repetition rate. This highlights the potential to tune the core W level simply by adjusting the granule pacing frequency. The success of this strategy is exemplified by discharge #85019, shown in panels (*c*)–(*e*). Continuous pacing with discrete Li injection (panel (*c*)) maintained high-frequency (∼100–500 Hz) small ELMs (panel (*d*)), resulting in a sustained low level of W concentration (panel (*e*), orange) and, consequently, high energy confinement (panel (*e*), black, H98 ≈ 1.0–1.1). This demonstrates that a sufficient frequency of small, relatively benign ELMs can effectively replicate or even surpass the impurity control function of infrequent large ELMs.

3.7. Core W expulsion via triggered small ELMs

A critical factor determining the effectiveness of core impurity control is the radial penetration depth of the ELM perturbation. Figure 11 investigates this by examining the time evolution of density-normalized emission brightness for various W charge states (measured by fast EUV) following different ELM events. The impact of the ELMs is most clear and prompt on W ions residing in the pedestal and outer mid-radius regions. As shown in panels (*b*)–(*d*), single-triggered small ELMs (thin vertical orange lines) cause immediate and distinct reductions in the emission from W^{26+} through W^{32+}. These small ELMs also induce a noticeable, albeit more modest, reduction in emission from mid-radius ions such as W^{38+} (panels (*e*)–(*g*)). For the core-localized W ions (W^{43+} to W^{45+}, panels (*h*)–(*j*)), the immediate response to a single, small ELM can be obscured by measurement noise. However, the underlying trend, made clearer by applying a Savitzky-Golay smoothing filter to the data (overlaid in the figure), reveals an appreciable reduction in core W ion concentrations. This effect is most pronounced following the cluster of ELMs at $t \approx 6.68$ s (thick orange vertical line). While the drop after a single triggered ELM is modest, further evidence for the deep penetration of these events comes from other discharges. For instance, a triggered ELM in discharge #85018 ($t \approx 4.2$ s, figure 12) leads to a relatively clear and straightforward drop for the highly-charged W ions (W^{41+}, W^{42+}, W^{43+}). Taken together, these observations provide compelling evidence that these triggered small ELMs, despite their modest D_α size, induce perturbations that penetrate sufficiently deep

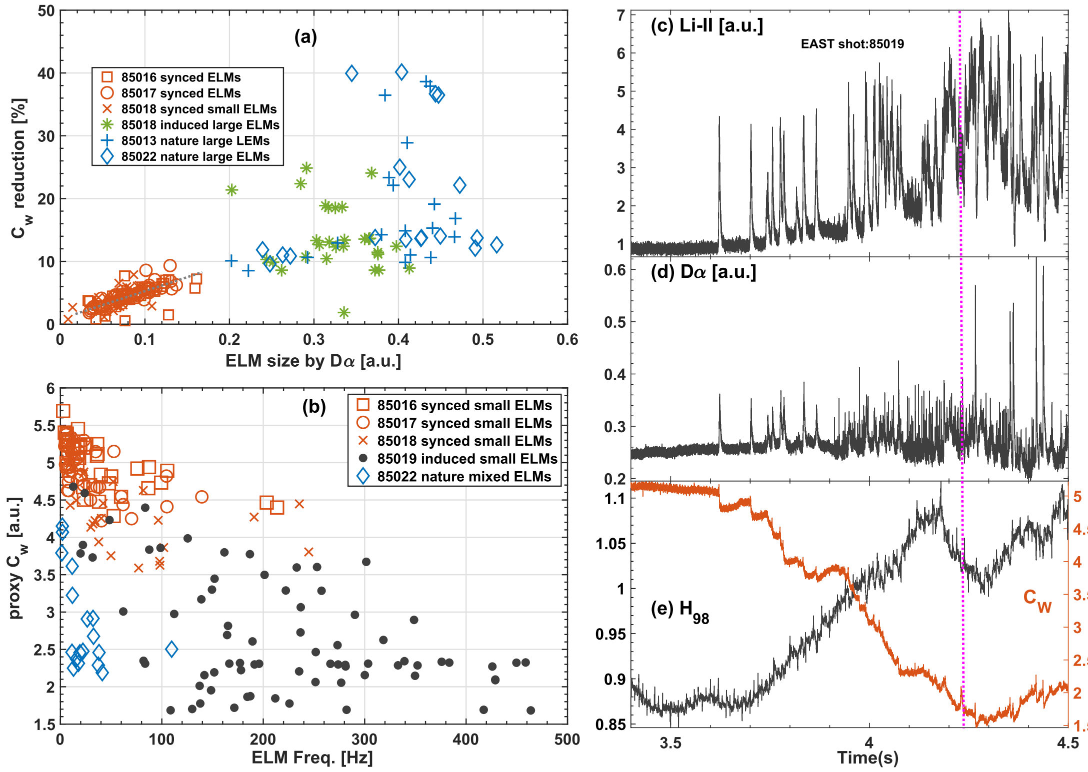

Figure 10. Impact of ELM frequency and size on tungsten concentration and H98 factor. Orange markers indicate Li-triggered small ELMs (#85016, #85017, #85018 Phase II). Blue markers correspond to natural large ELM discharges (#85013, #85022). Green marker indicates induced large ELMs in the mixed phase of #85018. (*a*) Fractional W concentration drop per ELM versus ELM size (D-alpha amplitude). (*b*) Average W concentration versus average ELM frequency, showing effective W control at high frequency. (*c*)–(*e*) Time traces from discharge #85016: (*c*) Li-II signal, (*d*) D-alpha signal showing high-frequency small ELMs, (e) Resulting in low W concentration (orange) and high H98 factor (black). The vertical pink dotted line in panels (*c*)–(*e*) indicates the time of the first large ELM appearance in discharge #85019, marking the transition to the mixed ELM regime. Li injection in this discharge begins at t ∼ 3.62 s, corresponding to the first Li-II spike shown in panel (*c*).

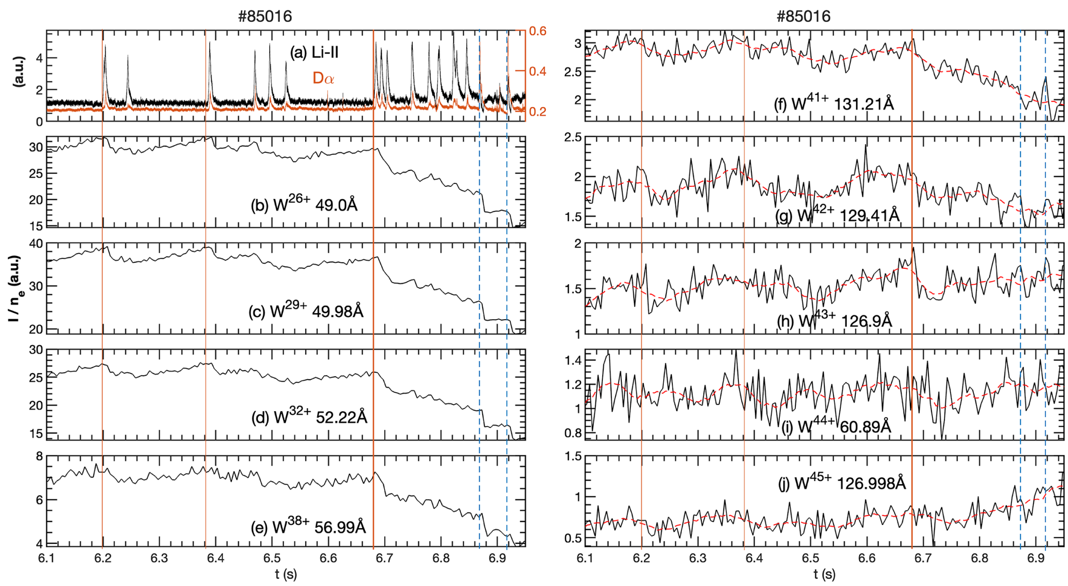

Figure 11. Time evolution of density-normalized tungsten ion emission brightness following different ELM events. Thin vertical orange lines: single-triggered small ELMs. Thick vertical orange line: a cluster of triggered small ELMs. Dashed vertical blue lines: single spontaneous large ELMs. (*a*) Li-II and Dalpha emissions identify injection and ELMs. (*b*)–(*j*) Normalized emission intensity for different W charge states, grouped approximately by location: inner pedestal or outer mid-radius (*b*), mid-radius (*c*)–(*g*), core (*h*)–(*j*). To clarify the underlying trends in the presence of noise, dashed red lines obtained by a standard Savitzky-Golay smoothing filter are superimposed on the core ion data in panels (*f*)–(*j*).

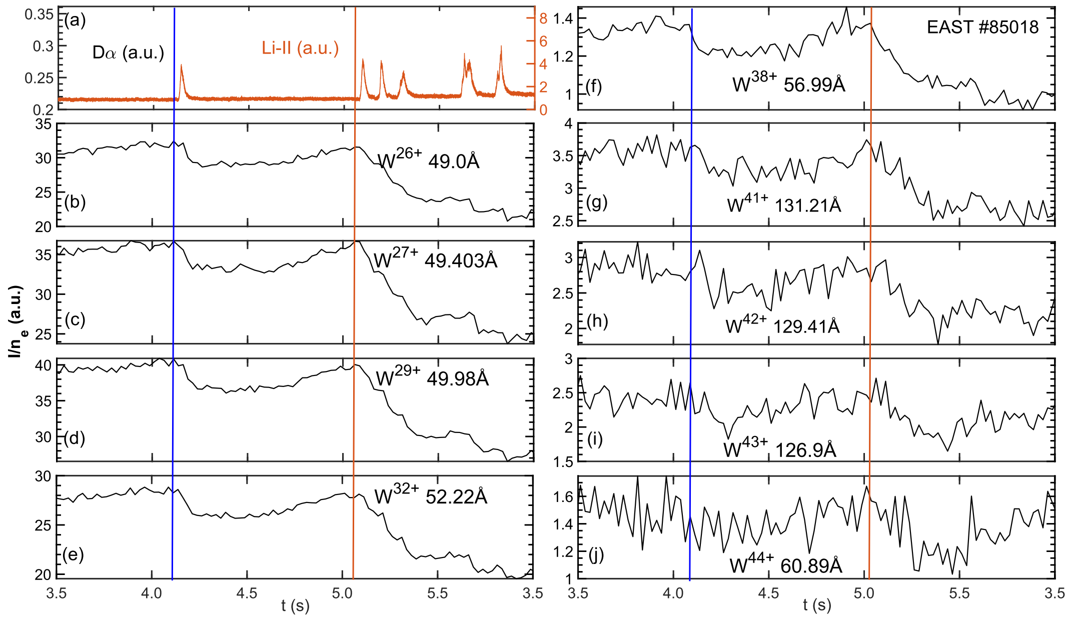

Figure 12. Time evolution of density-normalized tungsten ion emission brightness following different ELM events in discharge 85018. The vertical blue lines represent single-triggered small ELMs. The vertical orange lines indicate a cluster of triggered small ELMs. (*a*) Li-II and Dalpha emissions identify injection and ELMs. (*b*)–(*j*) Normalized emission intensity for different W charge states.

(at least to $\rho \approx 0.3$–0.5) to directly influence W transport well inside the pedestal top. This capability for core interaction is fundamental to their success in alleviating core W accumulation. It is important to distinguish the observations in figure 11 from those in figure 5(*d*). Figure 11 illustrates the small, instantaneous impact of discrete ELMs on the core ions within a given plasma state. In contrast, figure 5(*d*) shows that the large, time-averaged, cumulative effect during continuous injection has significantly modified the background plasma profiles (e.g. higher core T_e and lower pedestal n_e), leading to a much larger and more sustained reduction in core tungsten. The two figures thus represent different temporal aspects of the same underlying physical process: the immediate, small effect of a single ELM versus the large, integrated effect of many ELMs.

Complementary evidence comes from fast profile diagnostics shown in figure 13, tracking T_e (ECE) and n_e (reflectometry) evolution following three triggered small ELMs. The ECE data (panels (*a*)–(*e*)) reveal prompt (<1 ms) drops in electron temperature that clearly penetrate deep into the plasma, being readily observable down to $\rho \approx 0.4$ (panel (*a*)). The reflectometry data (panels (*f*)–(*j*)) show distinct density drops associated with the ELM in the pedestal and SOL regions (panels (*h*)–(*j*)). While resolving density perturbations deeper in the core (e.g. panel (*f*), $\rho \approx 0.57$) is challenging due to diagnostic limitations, the observed drops at the edge are consistent with particle expulsion. The lack of any *density increase* following the granule injection further supports the idea of minimal net fueling. Taken together, the prompt core T_e perturbation seen in ECE and the reduction of mid-radius and core W ion populations seen in EUV spectroscopy provide compelling evidence that these triggered small ELMs, despite their modest D_α signature, induce perturbations that penetrate sufficiently deep (at least to $\rho \approx 0.3$–0.5) to directly influence W transport well inside the pedestal top. This capability for core interaction is fundamental to their success in alleviating core W accumulation.

4. Discussion

4.1. Triggering mechanism and role of X-point injection

The underlying mechanism for ELM triggering by granules involves the creation of a strong, localized perturbation by the ablating material [46, 55]. When this occurs in the steep gradient region of the pedestal, it can locally destabilize MHD modes, primarily by exceeding the peeling–ballooning stability boundary. The rapid triggering (~4 ms, figure 8) suggests a fast MHD destabilization. The choice of injection near the *X*-point appears particularly advantageous. The significant magnetic flux expansion in this region amplifies the poloidal extent of the perturbation caused by the radially shallow granule penetration. This effectively creates a larger-scale disturbance along the sensitive separatrix and pedestal foot region compared to what a similar granule might produce if injected at the midplane. Perturbations localized near the separatrix, particularly on the low-field side, may efficiently drive ballooning-type instabilities or turbulence due to unfavorable curvature and strong gradients. Recent nonlinear MHD simulations using BOUT++ indeed suggest that the

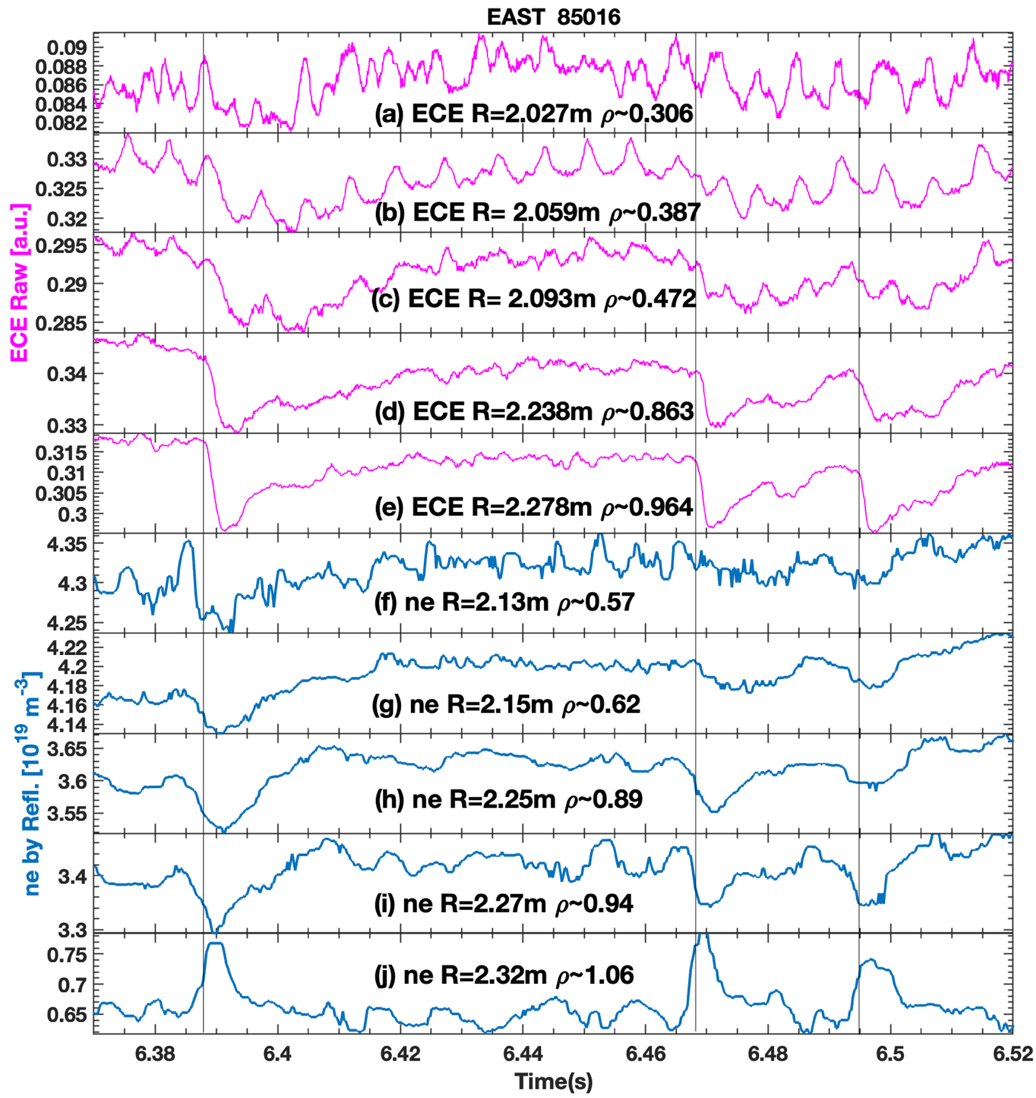

Figure 13. Evolution of electron temperature (from ECE) and density (from reflectometry) at different normalized minor radius locations (ρ) following three triggered small ELMs (indicated by vertical lines). (*a*)–(*e*) ECE raw data showing T_e evolution from core ($\rho \approx 0.4$) to pedestal top ($\rho \approx 0.96$), indicating deep thermal perturbation. (*f*)–(*j*) Density evolution from mid-radius ($\rho \approx 0.57$) to SOL ($\rho \approx 1.06$), showing density expulsion at the edge/SOL, consistent with minimal net fueling from the granule.

pressure perturbation near the separatrix plays a key role in destabilizing edge modes and triggering ELM-like events [56].

4.2. Compatibility, control, and comparison with the QCE

The experiments revealed different modes of interaction with the baseline EDA H-mode. During the discrete injection phase (Phase II), triggered small ELMs coexisted with the QCM, suggesting that this technique can supplement existing transport mechanisms to enhance impurity control without necessarily disrupting the underlying plasma regime. In contrast, the transition to continuous injection and mixed ELMs (Phase III) led to suppression of the QCM, likely due to the significant profile modifications (lower n_e, higher T_e) resulting from the more intense ELM activity. This highlights a potential pathway to transition from a QCM-dominated transport regime to an ELM-controlled one.

The observed lack of significant plasma density increase during Li injection (figures 3(*d*) and 6(*a*)), coupled with density drops following individual ELMs (figures 12(*f*)–(*j*)), strongly indicates minimal net fueling. This is attributed to the combination of shallow particle deposition near the *X*-point and the efficient expulsion by the promptly triggered ELM. This minimizes potential complications from unwanted density rises [28, 32, 57] and also implies negligible fuel dilution from the injected lithium, as the Li ions are largely expelled before significant core accumulation can occur. An interesting aspect is the observed deep penetration of the triggered small ELM's effects (T_e to $\rho \approx 0.4$, W ions to $\rho \approx 0.5$–0.6), as shown in section 3.7. The connection between edge and core needs to be explored in the future.

The nature of the triggered small ELMs invites comparison with the QCE regime [10]. Both scenarios achieve effective particle and impurity exhaust via small, frequent transport events, avoiding large Type-I ELMs. QCE is understood to arise from the plasma edge self-regulating near the local ideal ballooning limit, leading to intrinsic high-frequency modes or filaments. The triggered small ELMs induced here are due to the external perturbation from the granule injection.

4.3. Optimized operation and future prospects

Future work should focus on refining the IPD technology for more precise control over granule timing and velocity to enable sophisticated feedback algorithms. Assessing the long-term effects of Li (or alternative low-Z materials like B) on PFCs and fuel retention in sustained scenarios is necessary. Minimizing the associated increase in gross divertor sputtering (observed in Phase III) through optimization of ELM frequency and size requires further study. Extending the technique to other ELM-suppressed regimes, particularly QH-mode where impurity accumulation can be limiting [23], is a critical next step to evaluate its broader applicability and compatibility with modes like the EHO. Integrating real-time W diagnostics with the IPD offers the prospect of adaptive impurity control, triggering ELMs only when necessary.

5. Summary

This manuscript reports the successful demonstration of on-demand ELM triggering for active tungsten control in ELM-absent EDA H-mode plasmas on EAST using submillimeter lithium granule injection near the *X*-point. The key findings are:

1. **Robust & controllable triggering**: *X*-point Li granule injection reliably triggered ELMs (∼100% efficiency) with frequency controlled by the injection rate (5–250 Hz).
2. **Small ELM pacing regime**: Discrete injection paced small ELMs at high frequency (up to 500 Hz), effectively controlling W accumulation with minimal plasma perturbation and negligible net fueling or dilution.
3. **Compatibility & transition**: Triggered small ELMs coexisted with the EDA H-mode's QCM. Higher frequency/continuous injection suppressed the QCM and induced mixed ELMs, providing stronger W expulsion but with larger events.
4. **Tungsten expulsion & confinement**: Triggered ELMs significantly reduced W concentration (up to 60%) and radiated power, leading to increased core temperatures (T_e up by ∼40%, T_i up by 20%–40%) and improved energy confinement (H98(y,2) from ∼0.87 to ∼1.12).
5. **Core penetration:** Triggered small ELMs induced prompt perturbations deep into the core (T_e at $\rho \approx 0.4$, W ions at $\rho \approx 0.5$–0.6), crucial for flushing core-accumulated W.
6. **Optimized operation:** High-frequency small ELM pacing emerges as an attractive scenario, offering sufficient W control via controllable, benign ELMs, leading to improved plasma performance without large ELM drawbacks or significant fueling effects.

These results demonstrate that externally paced, small ELMs triggered by Li granule injection offer a promising and flexible method for managing impurity accumulation in ELM-suppressed H-mode scenarios. This technique provides a pathway to simultaneously achieve good energy confinement and acceptable core impurity levels, which is critical for sustained high-performance operation in NSTX-U and future fusion reactors like ITER.

Acknowledgment

The authors would like to thank the EAST team for their support of the experiments and gratefully acknowledge Tanmay Macwan (LLNL), Mao Li (DLUT), Jason Parisi (PPPL), and Adam Mclean (LLNL) for their valuable discussions. This work was supported in part by the U.S. Department of Energy under Contract No. DE-AC02-09CH11466, and in part by the National Key Research and Development Program of China (2024YEF03000200, 2022YFE03180400, 2022YFE03040003, 2022YFE03010002, 2022YFE03100003, 2022YFE03130004, 2024YFE03020003, 2024YFE03250300), the National Natural Science Foundation of China (12205336, 12475208, 12475207), and the Strategic Priority Research Program of Chinese Academy of Sciences under Grant No. XDB0790102, Provincial Natural Science Foundation of Anhui (2408085J002, 2408085QA007), as well as the Interdisciplinary and Collaborative Teams of CAS. The data that support the findings of this study are available from the corresponding authors upon reasonable request. Raw data were generated at the EAST facility.

ORCID iDs

Z. Sun 0000-0002-7224-3592
R. Maingi 0000-0003-1238-8121
Y.X. Cheng 0000-0002-9195-2757
Y.Z. Qian 0009-0001-9858-8898
W. Xu 0000-0001-8619-6953
Z. Wang 0009-0007-6857-1431
Y.F. Wang 0000-0002-0368-9566
T. Zhang 0000-0002-1555-6226
L. Chen 0000-0002-7176-4978
W. Wang 0009-0007-6479-6326
D.G. Wu 0000-0002-2457-1049
K. Jia 0009-0000-0558-0006
H.Q. Wang 0000-0003-1920-2799
R. Lunsford 0000-0003-3588-6801
A. Diallo 0000-0002-0706-060X
G.Z. Zuo 0000-0002-4149-089X

References

[1] Connor J.W. 1998 A review of models for ELMs *Plasma Phys. Control. Fusion* **40** 191
[2] Loarte A. *et al* 2014 Progress on the application of ELM control schemes to ITER scenarios from the non-active phase to DT operation *Nucl. Fusion* **54** 033007

[3] Pütterich T., Dux R., Janzer M.A. and McDermott R.M. 2011 ELM flushing and impurity transport in the H-mode edge barrier in ASDEX Upgrade *J. Nucl. Mater.* **415** S334
[4] Wade M.R., Burrell K.H., Leonard A.W., Osborne T.H. and Snyder P.B. 2005 Edge-localized-mode–induced transport of impurity density, energy, and momentum *Phys. Rev. Lett.* **94** 225001
[5] Leonard A.W. 2014 Edge-localized-modes in tokamaks *Phys. Plasmas* **21** 090501
[6] Evans T.E. *et al* 2006 Edge stability and transport control with resonant magnetic perturbations in collisionless tokamak plasmas *Nat. Phys.* **2** 419
[7] Sun Z. *et al* 2021 Type-I ELM mitigation by continuous lithium granule gravitational injection into the upper tungsten divertor in EAST *Nucl. Fusion* **61** 066022
[8] Sun Z. *et al* 2021 Suppression of edge localized modes with real-time boron injection using the tungsten divertor in EAST *Nucl. Fusion* **61** 014002
[9] Maingi R. *et al* 2009 Edge-localized-mode suppression through density-profile modification with lithium-wall coatings in the national spherical torus experiment *Phys. Rev. Lett.* **103** 075001
[10] Faitsch M., Eich T., Harrer G.F., Wolfrum E., Brida D., David P., Dunne M., Gil L., Labit B. and Stroth U. 2023 Analysis and expansion of the quasi-continuous exhaust (QCE) regime in ASDEX Upgrade *Nucl. Fusion* **63** 076013
[11] Greenwald M. *et al* 1999 Characterization of enhanced D alpha high-confinement modes in Alcator C-mod *Phys. Plasmas* **6** 1943
[12] Gil L. *et al* 2020 Stationary ELM-free H-mode in ASDEX Upgrade *Nucl. Fusion* **60** 054003
[13] Zhang T. *et al* 2017 Outward particle transport by coherent mode in the H-mode pedestal in the Experimental Advanced Superconducting Tokamak (EAST) *Plasma Phys. Control. Fusion* **59** 065012
[14] Ye Y. *et al* 2017 A stationary long-pulse ELM-absent H-mode regime in EAST *Nucl. Fusion* **57** 086041
[15] Macwan T. *et al* 2024 ELM-free enhanced Dα H-mode with near zero NBI torque injection in DIII-D tokamak *Phys. Plasmas* **31** 122503
[16] Whyte D.G. *et al* 2010 I-mode: an H-mode energy confinement regime with L-mode particle transport in Alcator C-Mod *Nucl. Fusion* **50** 105005
[17] Burrell K.H. *et al* 2001 Quiescent double barrier high-confinement mode plasmas in the DIII-D tokamak *Phys. Plasmas* **8** 2153
[18] Field A.R. *et al* 2021 The impact of fuelling and W radiation on the performance of high-power, ITER-baseline scenario plasmas in JET-ILW *Plasma Phys. Control. Fusion* **63** 095013
[19] Fedorczak N. *et al* 2015 Tungsten transport and sources control in JET ITER-like wall H-mode plasmas *J. Nucl. Mater.* **463** 85
[20] Dux R., Janzer A. and Pütterich T. (ASDEX Upgrade Team) 2011 Main chamber sources and edge transport of tungsten in H-mode plasmas at ASDEX Upgrade *Nucl. Fusion* **51** 119501
[21] Canik J.M. *et al* 2010 On demand triggering of edge localized instabilities using external nonaxisymmetric magnetic perturbations in toroidal plasmas *Phys. Rev. Lett.* **104** 045001
[22] Jackson G.L. *et al* 1991 Regime of very high confinement in the boronized DIII-D Tokamak *Phys. Rev. Lett.* **67** 3098
[23] Ernst D., Bortolon A., Chen X., King J., Nelson A., Battaglia D. and Hubbard A. (the 2022 JRT Team) 2023 Results of the 2022 U.S. joint research target on intrinsically Non-ELMing enhanced confinement regimes *65th Annual Meeting of the APS Division of Plasma Physics* (*Denver, Colorado, US, 30 October–3 November 2023*) (available at: https://meetings.aps.org/Meeting/DPP23/Session/BI02.6) p BI02.006
[24] Pitts R.A. *et al* 2019 Physics basis for the first ITER tungsten divertor *Nucl. Mater. Energy* **20** 100696
[25] Pütterich T. *et al* 2013 Observations on the W-transport in the core plasma of JET and ASDEX Upgrade *Plasma Phys. Control. Fusion* **55** 124036
[26] Angioni C. 2021 Impurity transport in tokamak plasmas, theory, modelling and comparison with experiments *Plasma Phys. Control. Fusion* **63** 073001
[27] Field A.R. *et al* 2022 Peripheral temperature gradient screening of high-Z impurities in optimised 'hybrid' scenario H-mode plasmas in JET-ILW *Nucl. Fusion* **63** 016028
[28] Lang P.T. *et al* 2003 ELM frequency control by continuous small pellet injection in ASDEX Upgrade *Nucl. Fusion* **43** 1110
[29] Baylor L.R. *et al* 2013 Reduction of edge-localized mode intensity using high-repetition-rate pellet injection in tokamak H-mode plasmas *Phys. Rev. Lett.* **110** 245001
[30] Bortolon A. *et al* 2016 High frequency pacing of edge localized modes by injection of lithium granules in DIII-D H-mode discharges *Nucl. Fusion* **56** 056008
[31] Sun Z. *et al* 2018 First results of ELM triggering with a multichamber lithium granule injector into EAST discharges *IEEE Trans. Plasma Sci.* **46** 1076
[32] Lunsford R. *et al* 2018 Injected mass deposition thresholds for lithium granule instigated triggering of edge localized modes on EAST *Nucl. Fusion* **58** 036007
[33] Lunsford R. *et al* 2018 ELM frequency enhancement and discharge modification through lithium granule injection into EAST H-modes *Nucl. Fusion* **58** 126021
[34] Li M., Sun Z., Sun J., Chang H. and Xia T. 2024 Simulation of Li-pellet triggered ELMs in EAST with an impurity model implemented under BOUT++ framework *Nucl. Fusion* **65** 026007
[35] Loarte A., Pitts R., Wauters T., Nunes I., Köchl F., Polevoi A., Kim S., Lehnen M., Artola J. and Chen L. 2024 Initial evaluations in support of the new ITER baseline and research plan *Technical Report No. ITR-24-004* (available at: www.iter.org/sites/default/files/media/2024-04/itr-24-004-baseline-ok.pdf)
[36] Snipes J.A. *et al* 2024 Initial design concepts for solid boron injection in ITER *Nucl. Mater. Energy* **41** 101809
[37] Wan B.N. *et al* 2022 Advances in the long-pulse steady-state high beta H-mode scenario with active controls of divertor heat and particle fluxes in EAST *Nucl. Fusion* **62** 042010
[38] Chen X.H. *et al* 2021 The impact of ELM mitigation on tungsten source in the EAST divertor *Nucl. Fusion* **61** 046046
[39] Zhang L. *et al* 2015 A fast-time-response extreme ultraviolet spectrometer for measurement of impurity line emissions in the Experimental Advanced Superconducting Tokamak *Rev. Sci. Instrum.* **86** 123509
[40] Zhang L. *et al* 2019 A space-resolved extreme ultraviolet spectrometer for radial profile measurement of tungsten ions in the Experimental Advanced Superconducting Tokamak *Nucl. Instrum. Methods Phys. Res. A* **916** 169
[41] Yang X., Zhang L. and Xu Z. 2017 Preliminary result of impurity density evaluation on EAST *Proc. of A3 Foresight Program Seminar on Critical Physics Issues Specific to Steady State Sustainment of High-performance Plasmas 2016* (*Yinchuan, China, 17–20 May 2016*) p 241 (available at: https://inis.iaea.org/records/9d5zr-thy53)
[42] Asmussen K., Fournier K.B., Laming J.M., Neu R., Seely J.F., Dux R., Engelhardt W. and Fuchs J.C. (ASDEX Upgrade Team) 1998 Spectroscopic investigations of tungsten in the

EUV region and the determination of its concentration in tokamaks *Nucl. Fusion* **38** 967
[43] Cheng Y. *et al* 2025 The observation of tungsten unresolved transition arrays spectra at high electron temperature in Experimental Advanced Superconducting Tokamak (EAST) plasma *Plasma Fusion Res.* **20** 2402010
[44] Nagy A., Bortolon A., Mauzey D.M., Wolfe E., Gilson E.P., Lunsford R., Maingi R., Mansfield D.K., Nazikian R. and Roquemore A.L. 2018 A multi-species powder dropper for magnetic fusion applications *Rev. Sci. Instrum.* **89** 10K121
[45] Mansfield D.K. *et al* 2013 First observations of ELM triggering by injected lithium granules in EAST *Nucl. Fusion* **53** 113023
[46] Huysmans G.T.A., Pamela S., van der Plas E. and Ramet P. 2009 Non-linear MHD simulations of edge localized modes (ELMs) *Plasma Phys. Control. Fusion* **51** 124012
[47] Mossessian D.A., Snyder P., Hubbard A., Hughes J.W., Greenwald M., LaBombard B., Snipes J.A., Wolfe S. and Wilson H. 2003 High-confinement-mode edge stability of Alcator C-mod plasmas *Phys. Plasmas* **10** 1720
[48] Kamiya K. *et al* 2004 High, recycling steady H-mode regime in the JFT-2M tokamak *Plasma Phys. Control. Fusion* **46** A157
[49] OPEN-ADAS (available at: http://open.adas.ac.uk)
[50] Loch S.D., Ludlow J.A., Pindzola M.S., Whiteford A.D. and Griffin D.C. 2005 Electron-impact ionization of atomic ions in the W isonuclear sequence *Phys. Rev. A* **72** 052716
[51] Pütterich T., Neu R., Dux R., Whiteford A.D. and O'Mullane M.G. 2008 Modelling of measured tungsten spectra from ASDEX Upgrade and predictions for ITER *Plasma Phys. Control. Fusion* **50** 085016
[52] Fujii K., Kato D., Nakamura N., Goto M., Morita S. and Hasuo M. 2017 Experimental evaluation of fractional abundance data for W^{23+}–W^{28+} *J. Phys. B* **50** 055004
[53] Oishi T., Morita S., Kato D., Murakami I., Sakaue H.A., Kawamoto Y. and Goto M. 2020 Observation of line emissions from Ni-like W^{46+} ions in wavelength range of 7–8 Å in the large helical device *Phys. Scr.* **96** 025602
[54] Angioni C., Fable E., Greenwald M., Maslov M., Peeters A.G., Takenaga H. and Weisen H. 2009 Particle transport in tokamak plasmas, theory and experiment *Plasma Phys. Control. Fusion* **51** 124017
[55] Futatani S., Huijsmans G., Loarte A., Baylor L.R., Commaux N., Jernigan T.C., Fenstermacher M.E., Lasnier C., Osborne T.H. and Pegourié B. 2014 Non-linear MHD modelling of ELM triggering by pellet injection in DIII-D and implications for ITER *Nucl. Fusion* **54** 073008
[56] Li N., Xu X.Q., Wang Y.F., Lin X., Yan N. and Xu G.S. 2022 Impact of pedestal density gradient and collisionality on ELM dynamics *Phys. Plasmas* **29** 122302
[57] Wang Z., Hoffbauer M.A., Hollmann E.M., Sun Z., Wang Y.M., Eidietis N.W., Hu J., Maingi R., Menard J.E. and Xu X.Q. 2019 Hollow pellet injection for magnetic fusion *Nucl. Fusion* **59** 086024